

---

# WIDE FIELD-OF-VIEW, LARGE-AREA LONG-WAVE INFRARED SILICON METALENSSES

---

A PREPRINT

**Hung-I Lin\***

Massachusetts Institute of Technology  
Cambridge, MA

**Jeffrey Geldmeier\***

Lockheed Martin Corporation  
Orlando, FL

**Erwan Baleine\***

Lockheed Martin Corporation  
Orlando, FL

**Fan Yang\***

Massachusetts Institute of Technology  
Cambridge, MA

**Sensong An**

Massachusetts Institute of Technology  
Cambridge, MA

**Ying Pan**

Massachusetts Institute of Technology  
Cambridge, MA

**Clara Rivero-Baleine<sup>†</sup>**

Lockheed Martin Corporation  
Orlando, FL  
rivcar21@hotmail.com

**Tian Gu<sup>†</sup>**

Massachusetts Institute of Technology  
Cambridge, MA  
gutian@mit.edu

**Juejun Hu**

Massachusetts Institute of Technology  
Cambridge, MA

July 25, 2023

## ABSTRACT

Long-wave infrared (LWIR, 8-12  $\mu\text{m}$  wavelengths) is a spectral band of vital importance to thermal imaging. Conventional LWIR optics made from single-crystalline Ge and chalcogenide glasses are bulky and fragile. The challenge is exacerbated for wide field-of-view (FOV) optics, which traditionally mandates multiple cascaded elements that severely add to complexity and cost. Here we designed and experimentally realized a LWIR metalens platform based on bulk Si wafers featuring 140° FOV. The metalenses, which have diameters exceeding 4 cm, were fabricated using a scalable wafer-level process involving photolithography and deep reactive ion etching. Using a metalens-integrated focal plane array, we further demonstrated wide-angle thermal imaging.

**Keywords** Wide field-of-view optics, metasurface, metalens, LWIR, fisheye lens

## 1 Introduction

LWIR, which coincides with the peak blackbody emission wavelengths of near-room-temperature objects, is strategically important to wide-ranging imaging applications spanning night vision, remote sensing, robotics, industrial process monitoring, building inspection, automotive sensing, gas detection, and beyond. Since most classical optical materials such as oxide glasses and polymers become opaque at LWIR due to phonon absorption, traditional LWIR optics resort to specialty materials such as single-crystalline Ge and chalcogenide glasses. These materials either incur a high cost to manufacture (Ge), or are mechanically fragile (chalcogenide glasses). Moreover, classical refractive optics made from these materials (Ge in particular) are temperature-sensitive due to thermo-optic focal drift. The challenges are

---

\*These authors contribute equally to this work

<sup>†</sup>Correspondence

further exacerbated when it comes to applications demanding a wide field-of-view (WFOV), since classical WFOV infrared optics entail a compound lens architecture comprising multiple (in general 4 or more) stacked optical elements to suppress coma aberration[1]. As a result, even LWIR lenses with a moderate FOV of around  $60^\circ$  each cost well above \$1,000 off-the-shelf.

Optical metasurfaces provide an alternative to classical refractive optics through modulation of the amplitude, phase, and polarization state of the wavefront using sub-wavelength nanostructures customarily termed meta-atoms [2, 3, 4, 5, 6, 7, 8, 9, 10, 11, 12]. While a large collection of metalenses have been implemented at visible and near-infrared wavelengths, relatively few demonstrations targeted the LWIR regime. Pioneering work by several groups have realized silicon-based LWIR metalenses [13, 14, 15, 16]. Using Si as the metasurface material is advantageous in that it is amenable to large-area wafer-level manufacturing processes, and that deep reactive ion etching (DRIE) can produce high aspect ratio Si meta-atom structures ideal for large optical phase coverage and potentially dispersion engineering [17]. Si wafers prepared using the common Czochralski method, however, are known to exhibit a strong optical absorption band centering at  $9 \mu m$  wavelength due to the presence of oxygen impurity [18]. To mitigate the issue, Ge coupled with a ZnS antireflection layer has been adopted for metalens fabrication to suppress parasitic absorption across the LWIR band [19]. The challenge of coma aberration suppression and expanding the FOV has nonetheless not been tackled by these pioneering investigations except in a recent report[20]. More recently, metalens arrays comprising five lens, each covering a sub-section of the FOV, have been implemented to demonstrate LWIR imaging spanning a horizontal FOV exceeding  $60^\circ$  upon image stitching in post-processing [21]. The approach is however hardly scalable to WFOV applications, as a large FOV (e.g.  $100^\circ$ ) in both horizontal and vertical directions would require tens of individual metalenses, severely curtailing the optical throughput while escalating system complexity.

In this paper, we report the design and experimental demonstration of a WFOV metalens covering  $140^\circ$  circular FOV. The metalens assumed a simple architecture consisting of an optical aperture stop and a single-layer metasurface patterned in a float-zone Si wafer. The choice of float-zone Si contributes to suppression of the oxygen impurity absorption band while still enabling full leverage of industry-standard Si fabrication processes. Compared to other WFOV designs such as quadratic phase[22, 23, 24, 25, 26, 27, 28] and doublet metalenses[29, 30, 31, 32, 33, 34], the present architecture is simple and yet does not compromise the imaging quality or optical efficiency [35].

The rest of this paper is organized as follows. We will start with formulating the overarching analytical design approach. Two metalens designs were derived using the method, with an air gap and a ZnSe spacer, respectively. The former features a simpler construction whereas the latter has the advantage of enhanced FOV and imaging quality as predicted by our analytical theory and validated via numerical simulations. We then proceed to describe the fabrication protocols as well as experimental characterization of both metalenses.

## 2 Analytical WFOV metalens design

The WFOV metalens architecture consisting of an aperture and an all-silicon metasurface is schematically illustrated in Fig. 1a [36, 37, 38]. The monochromatic phase profiles of the metasurfaces are defined following [39]:

$$\phi(s) = \left(\frac{2\pi}{\lambda}\right) \int_0^s \left(-\sin\alpha(s) + \frac{s-d}{\sqrt{f^2 + (s-d)^2}}\right) ds \quad (1)$$

The corresponding RMS wavefront error is given by:

$$\sigma \approx \frac{3nL^2D^3|s-d|}{160 \left(f^2 + (s-d)^2\right) (L^2 + s^2)^{\frac{3}{2}}} \quad (2)$$

We note that the numerator in the expression above contains the factor  $|s-d|$ , which corresponds to the transverse offset between the incident position of the chief ray on the metasurface and the corresponding focal spot position (i.e., image height). In an image-space telecentric configuration, the term vanishes, yielding optimal image quality. Optimizing the metalens design therefore involves engineering its image height vs. incident angle relation to mimic the telecentric configuration. This can be accomplished by changing the refractive index  $n_{sub}$  of the spacer material, leveraging refraction at the air-spacer front surface as a practical means to modify the image height. Following this rationale, we examine the dependence of the RMS wavefront error for various spacer material refractive indices and thicknesses (Fig. 1b).

Guided by the theoretical insight, we have chosen ZnSe ( $n_{sub} = 2.40$  at  $10.6 \mu m$ ) as the spacer material. An air-gap design ( $n_{sub} = 1$ ) was also implemented for comparison. The detailed design parameters are tabulated in Table 1 and Fig. 1c plots the phase profiles of the designs.

Table 1: Metalens design parameters

	Wavelength	Aperture size	Air-gap/ZnSe thickness	Si substrate thickness
Air-gap	$10.6 \mu m$	$6 mm$	$7.5 mm$	$675 \mu m$
ZnSe	$10.6 \mu m$	$10 mm$	$44 mm$	$675 \mu m$
	Focal length	Metalens size	Image plane size	FOV
Air-gap	$12 mm$	$32 mm$	$21 mm$	$90^\circ$
ZnSe	$20 mm$	$48 mm$	$38 mm$	$140^\circ$

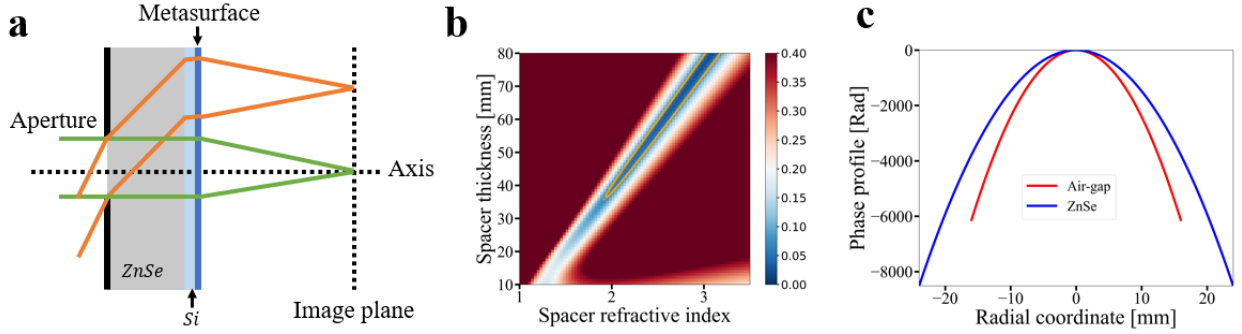


Figure 1: Analytically guided WFOV metalens design optimization. (a) Schematic illustration of the WFOV metalens configuration. (b) Averaged RMS wavefront error across the FOV for a range of spacer refractive indices and thicknesses. The simulations assume  $140^\circ$  FOV and  $20 mm$  focal length. To highlight the design space relevant to high-performance imaging, RMS wavefront errors greater or equal to  $0.4 \lambda$  are represented in the plot using a uniform crimson color. The orange contour encircles the design parameter space where the RMS wavefront error is smaller than  $0.0745 \lambda$ , which corresponds to the diffraction-limited performance criterion. (c) Phase profiles of the two metalens designs experimentally implemented in this study.

Next we translate the phase functions into actual metasurface layouts. The all-Si meta-atom structure is depicted in Fig. 2a inset, which is composed of  $12 \mu m$  tall pillars with a  $4 \mu m$  pitch etched into float-zone Si wafers. Full-wave electromagnetic simulations were performed using the Lumerical FDTD solver, and the transmittance and phase delay of the meta-atoms at  $10.6 \mu m$  wavelength as functions of the pillar diameter are shown in Figs. 2a-b. Eight meta-atoms with approximately  $\frac{\pi}{4}$  step size in phase were chosen to construct the metasurfaces. To optimize transmittance while suppressing phase error, we invoked a figure-of-merit function as the criterion to choose the meta-atom diameters [40, 41]. The eight selected meta-atom designs are summarized in Table 2.

Table 2: Meta-atom diameter, transmittance, and phase delay

Meta-atom index	1	2	3	4	5	6	7	8
Phase [ $^\circ$ ]	0	44	94	137	176	219	274	318
Transmittance	0.76	0.72	0.76	0.84	0.80	0.68	0.67	0.76
Diameter [ $\mu m$ ]	1.50	1.75	1.94	2.05	2.13	2.22	2.34	2.42

Based on the meta-atom characteristics, performances of the WFOV metalenses can be numerically evaluated using the Kirchhoff diffraction integral. The transverse and longitudinal focal spot intensity profiles of the two WFOV metalens designs at several different angles of incidence (AOIs) are presented in Fig. 3 and Fig. 4, respectively. The modulation

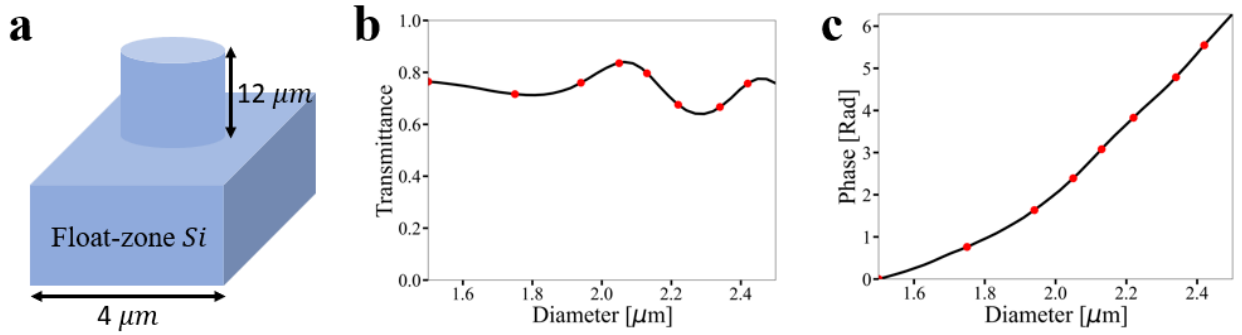


Figure 2: All-Si meta-atom design. (a) Transmittance and (c) phase delay responses of the meta-atoms with different pillar diameters. Inset depicts the meta-atom structure and the red dots denote the eight meta-atom designs selected to construct the metasurfaces.

transfer functions (MTFs) at different spatial frequencies were obtained through Fourier transform of the simulated point-spread-functions (PSFs) and are shown in Figs. 5a-b.

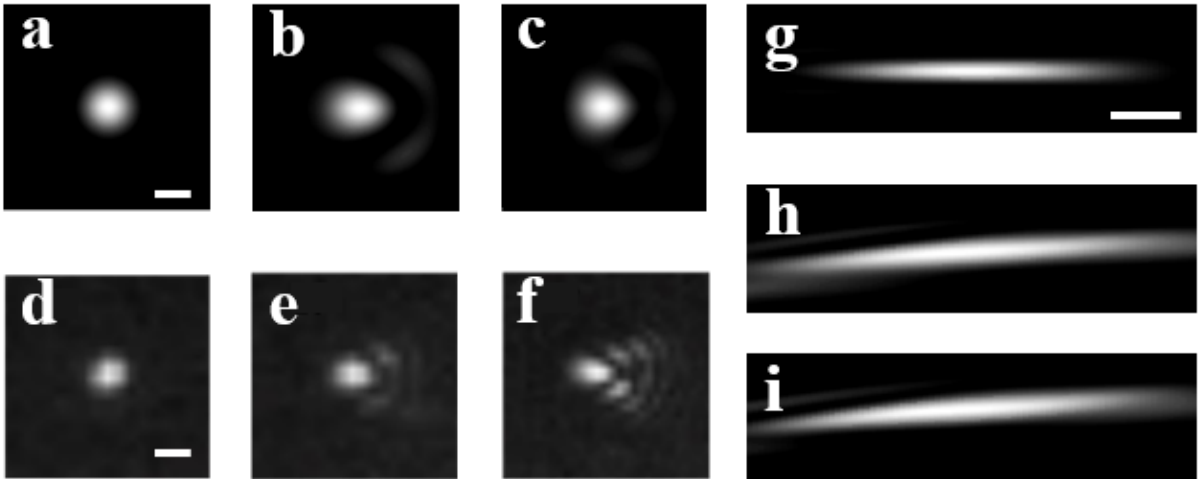


Figure 3: Focusing characteristics of the air-gap WFOV metalens at  $10.6 \mu\text{m}$  wavelength. (a)-(c) Simulated PSFs of the metalens at its image plane for AOIs of (a)  $0^\circ$ , (b)  $20^\circ$ , and (c)  $40^\circ$ . (Scale bar:  $20 \mu\text{m}$ .) (d)-(f) Measured PSFs of the metalens at its image plane for AOIs of (d)  $0^\circ$ , (e)  $20^\circ$ , and (f)  $40^\circ$ . (Scale bar:  $20 \mu\text{m}$ .) (g)-(i) Simulated longitudinal intensity profiles of the metalens focal spot at AOIs of (g)  $0^\circ$ , (h)  $20^\circ$ , and (i)  $40^\circ$ . (Scale bar:  $100 \mu\text{m}$ .)

We now characterize the focusing efficiencies and Strehl ratios of the WFOV metalenses at  $10.6 \mu\text{m}$  wavelength using the numerical results in Figs. 3 and 4. Here the focusing efficiency is defined as the fraction of power encircled within a diameter equaling five times the focal spot full-width-at-half-maximum (FWHM), normalized by the total incident power [37]. Figures 5c-d plot the two parameters as functions of AOI. The air-gap metalens has a focusing efficiency of 53% and a Strehl ratio of 0.63, both averaged over AOIs across the  $90^\circ$  FOV, whereas the ZnSe-spacer metalens claims a focusing efficiency of 50% and a Strehl ratio of 0.86, similarly averaged over AOIs throughout the entire  $140^\circ$  FOV. The enhanced focusing performance of the ZnSe-spacer lens over the air-gap design, evidenced by its diffraction-limited performance (Strehl ratio  $> 0.8$ ) over an extended FOV of  $140^\circ$ , validates our theoretical prediction.

### 3 Metalens fabrication

$2 \mu\text{m}$  thick SiN films were deposited by plasma-enhanced chemical vapor deposition (STS PECVD) on  $675 \mu\text{m}$  thick float zone Si wafers as a hard mask for DRIE. To define the metasurface patterns, a negative-tone photoresist (AZ

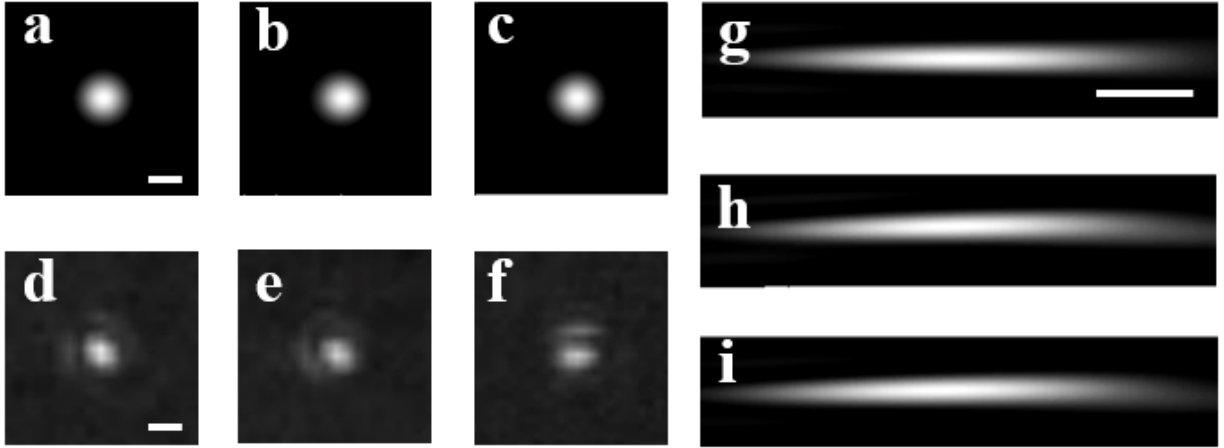


Figure 4: Focusing characteristics of the ZnSe-spacer WFOV metalens at  $10.6 \mu\text{m}$  wavelength. (a)-(c) Simulated PSFs of the metalens at its image plane for AOIs of (a)  $0^\circ$ , (b)  $30^\circ$ , and (c)  $70^\circ$ . (Scale bar:  $20 \mu\text{m}$ .) (d)-(f) Measured PSFs of the metalens at its image plane for AOIs of (d)  $0^\circ$ , (e)  $30^\circ$ , and (f)  $70^\circ$ . (Scale bar:  $20 \mu\text{m}$ .) (g)-(i) Simulated longitudinal intensity profiles of the metalens focal spot at AOIs of (g)  $0^\circ$ , (h)  $30^\circ$ , and (i)  $70^\circ$ . (Scale bar:  $100 \mu\text{m}$ .)

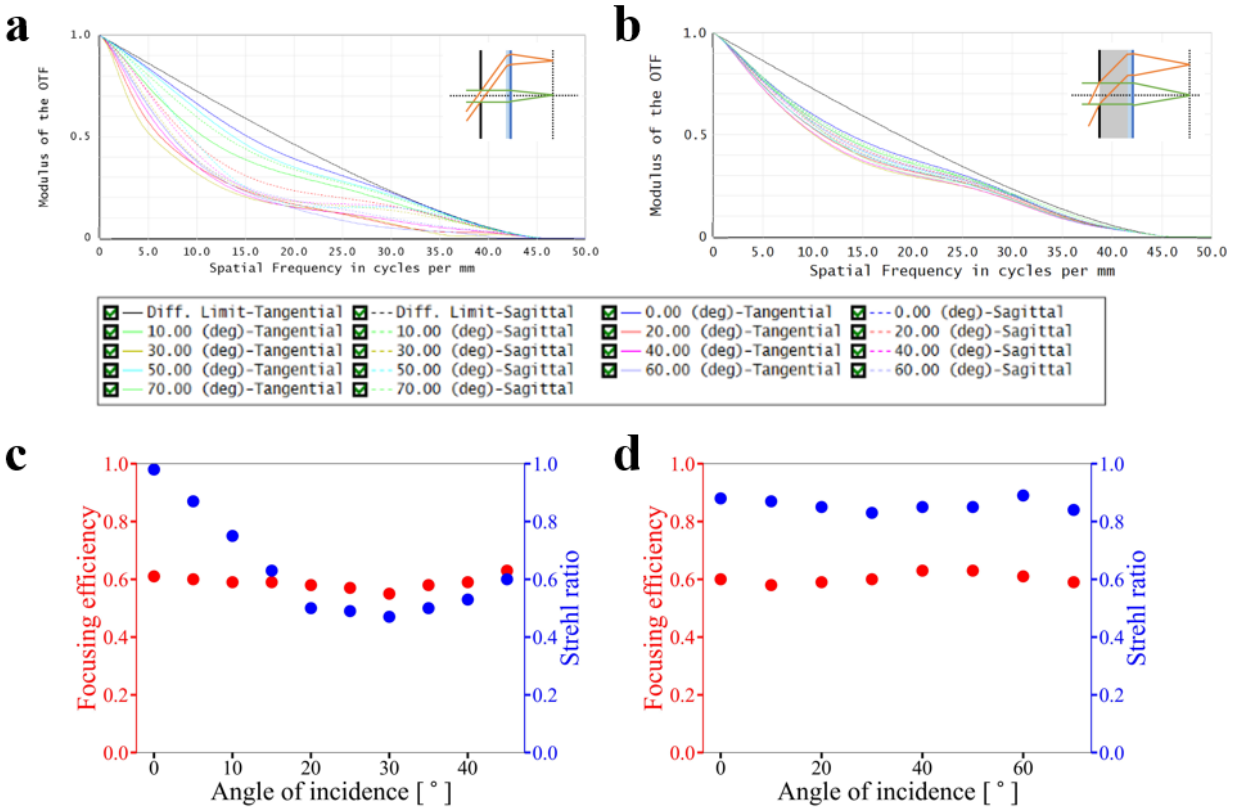


Figure 5: Metalens performance at  $10.6 \mu\text{m}$  wavelength. (a)-(b) Simulated MTFs of the (a) air-gap and (b) ZnSe-spacer metalenses at different AOIs. (c)-(d) Focusing efficiency and Strehl ratio of the (c) air-gap and (d) ZnSe-spacer metalenses as functions of AOI.

nLOF 2035) was spin-coated onto the substrates at 3000 revolutions per minute (rpm). The resist was soft-baked at  $115^\circ\text{C}$  for 1 minute, exposed on an MLA150 Maskless Aligner, and then post-exposure baked at  $115^\circ\text{C}$  for 1 minute.

The photoresist was developed by immersing the sample in Microposit MF-319 developer for 1 minute, followed by rinsing in deionized water. To etch the SiN hard mask, dry etching was performed using dual gas inlets with a mixture of SF<sub>6</sub> and C<sub>4</sub>F<sub>8</sub> (STS ICP RIE). The Bosch process was subsequently used to etch the Si meta-atoms (SPTS Rapier DRIE) before hard mask removal via buffered HF (BHF) wet etching to complete the fabrication process. To mitigate scalloping which is commonly associated with the Bosch process, we optimize 1) the gas flow ratio, which balances the etching and passivation effects; and 2) the etching loop time, which dictates the spatial period and severity of scalloping (Supplementary Information). Figure 6 shows images of the metasurfaces showing a low-roughness sidewall profile with minimal scalloping fabricated using the optimized parameters.

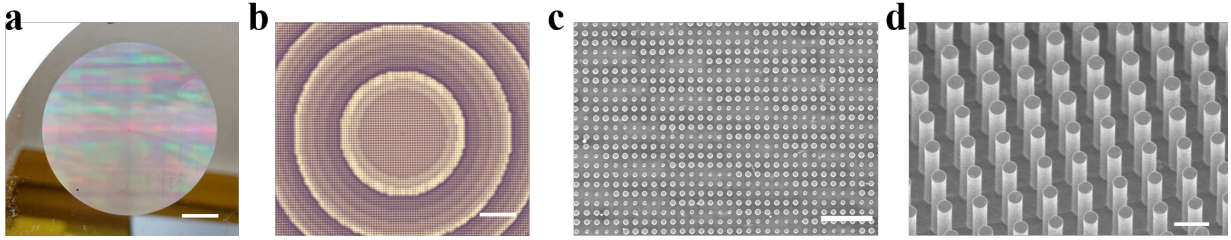


Figure 6: Images of fabricated metasurfaces. (a) A photo of a metasurface sample. (Scale bar: 10 mm.) (b) An optical micrograph of the metasurface. (Scale bar: 60  $\mu\text{m}$ .) (c) Top-view SEM image of the meta-atoms. (Scale bar: 20  $\mu\text{m}$ .) (d) Tilted-view SEM image showing scalloping-free sidewall profiles of the meta-atoms. (Scale bar: 4  $\mu\text{m}$ .)

#### 4 Metalens characterization and thermal imaging demonstration

The PSFs of the metalenses were characterized experimentally using a setup schematically depicted in Fig. 7a. A collimated 10.6  $\mu\text{m}$  CO<sub>2</sub> laser (LAGST, Access) was first attenuated and then expanded before being directed at the metalens and subsequently focused onto a microbolometer (Boson, FLIR). For field angles away from 0°, the metalens and the detector were tilted together, and the microbolometer also required lateral movement to span the much larger image plane. Several examples of the metalens PSFs at different AOIs are presented in Figs. 4d-f and Figs. 5d-f, respectively, showing excellent agreement between the measurement results and simulations. The monochromatic MTF performance of the metalenses at 10.6  $\mu\text{m}$  was measured using the collimated CO<sub>2</sub> laser and an interferometric wavefront sensor (SID4 DWIR, Phasics) schematically depicted in Fig. 7b. An aperture was placed in front of the metalenses in order to limit the collimated light bundle to the entrance pupil size. The Phasics camera was set to the focal mode, allowing measurements to be collected after direct diffraction from the lens. For the ZnSe metalens, an additional pinhole was placed near the focal plane to remove the zero order component. The corresponding MTFs are shown in Fig. 7c-d, indicating diffraction-limited performance in agreement with simulation predictions.

Finally, we demonstrated wide-angle thermal imaging using the metalens. The ZnSe metalens was mounted onto a microbolometer (Boson, FLIR) to form a thermal infrared camera. The experimental setup is shown in Fig. 8a. A hot plate was placed 0.53 meter away in front of the WFOV metalens to act as a LWIR illumination source. A cardboard 1.26 meters in length and perforated with 'EXTREME LOCKHEED MARTIN' patterns was placed in between the hot plate and the metalens, which blocked the blackbody radiation from the hot plate in all areas except within the inverse 'EXTREME LOCKHEED MARTIN' pattern. A 10.5  $\mu\text{m}$  filter with 0.2  $\mu\text{m}$  bandwidth was placed in front of the sensor. The captured image is presented in Fig. 8b covering 100° FOV. Since the image size is larger than the image sensor area, the bolometer had to be laterally translated with respect to the metalens and the resulting image sections were stitched to form Fig. 8b. We further compared the imaging results with those using an unfiltered blackbody source to quantify the impact of chromatic aberration, and the details were elaborated in the Supplementary Information.

#### 5 Conclusion

In this paper, we reported the design and experimental demonstration of metalenses operating at the LWIR band with an ultra-wide FOV of 140°. An analytical model was used to rationally guide the design of the metasurfaces as well as the lens spacer material choice. Following the designs, centimeter-scale metasurfaces were fabricated on float-zone silicon wafers using large-area photolithographic patterning and optimized DRIE protocols. Experimental characterization of the metalenses validated our theoretical design and demonstrated thermal imaging using a metalens-integrated infrared camera. Benefiting from its simple architecture, scalable fabrication process, and exceptional wide-FOV imaging

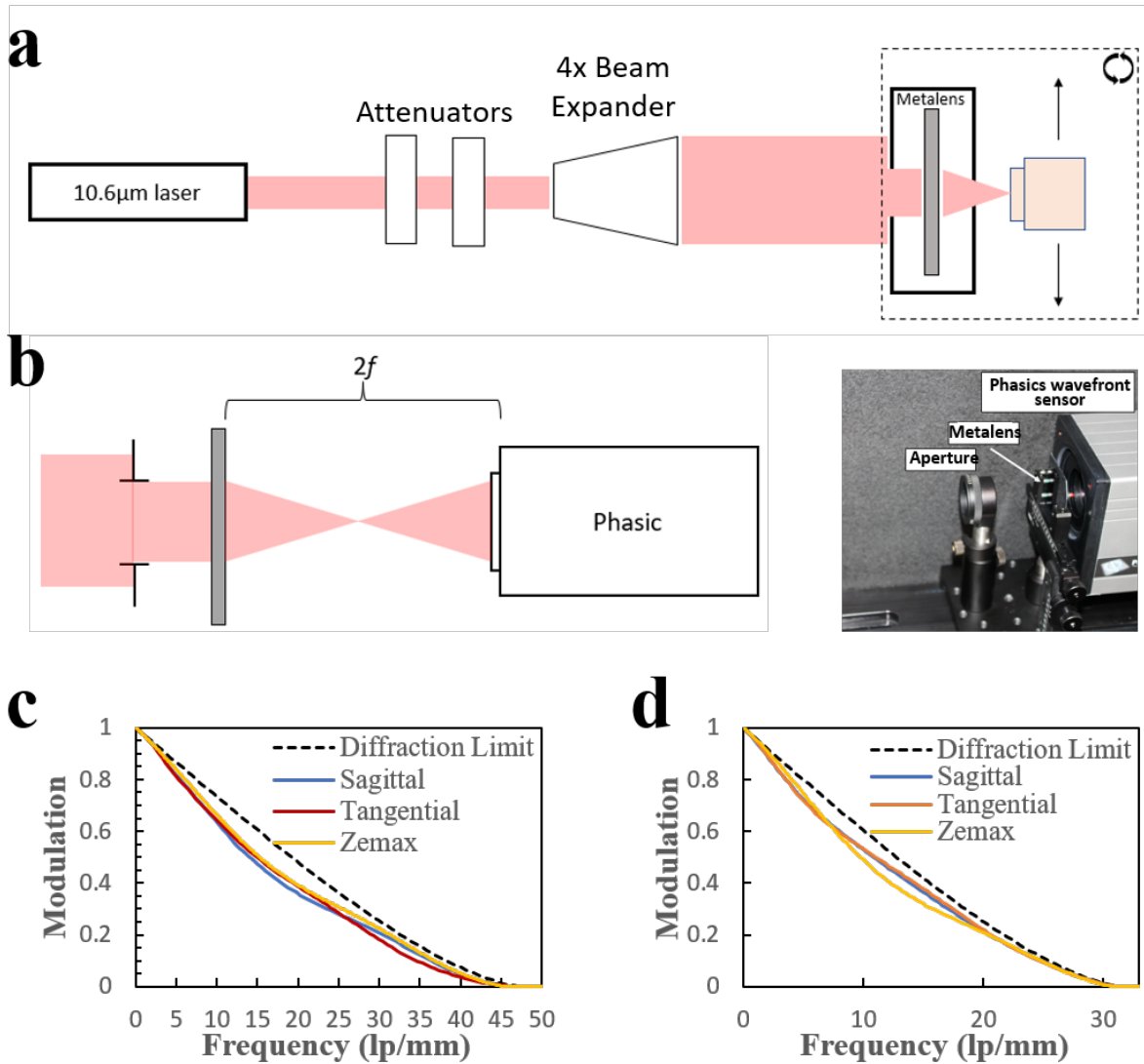


Figure 7: Experimental PSF and MTF measurements at  $10.6 \mu\text{m}$  wavelength. (a) Experimental setup for characterizing the metalens PSFs at different AOIs. (b) Experimental setup for wavefront measurement. (c)-(d) Normal-incidence MTFs of the (c) air-gap and (d) ZnSe metalens based on the wavefront measurement.

capability, the WFOV metalens technology potentially offers an appealing alternative to existing LWIR compound lens optics for applications covering night vision, spectroscopic sensing, environmental monitoring, and many others.

## 6 Acknowledgements

The authors acknowledge nanofabrication and characterization facility support provided by MIT.nano and the Center for Nanoscale Systems at Harvard University.

## 7 Funding

This work was supported by Lockheed Martin Corporation Internal Research and Development and Defense Advanced Research Projects Agency Defense Sciences Office Program: EXTREME Optics and Imaging (EXTREME) under



Figure 8: Wide-angle thermal imaging. (a) Experimental setup of the thermal imaging test. (b) Images taken by the thermal infrared camera integrated with the ZnSe-spacer metalens. Since the image size is larger than the bolometer sensor area, the bolometer was laterally translated with respect to the metalens and the resulting image sections were stitched.

agreement number HR00111720029. The views, opinions and/or findings expressed are those of the authors and should not be interpreted as representing the official views or policies of the Department of Defense or the US Government.

## References

- [1] Shimon Aburmad. Panoramic thermal imaging: challenges and tradeoffs. In *Infrared Technology and Applications XL*, volume 9070, pages 115–123. SPIE, 2014.
- [2] Nanfang Yu, Patrice Genevet, Mikhail A Kats, Francesco Aieta, Jean-Philippe Tetienne, Federico Capasso, and Zeno Gaburro. Light propagation with phase discontinuities: generalized laws of reflection and refraction. *science*, 334(6054):333–337, 2011.
- [3] Xingjie Ni, Naresh K Emani, Alexander V Kildishev, Alexandra Boltasseva, and Vladimir M Shalaev. Broadband light bending with plasmonic nanoantennas. *Science*, 335(6067):427–427, 2012.
- [4] Federico Capasso. The future and promise of flat optics: a personal perspective. *Nanophotonics*, 7(6):953–957, 2018.
- [5] Seyedeh Mahsa Kamali, Ehsan Arbabi, Amir Arbabi, and Andrei Faraon. A review of dielectric optical metasurfaces for wavefront control. *Nanophotonics*, 7(6):1041–1068, 2018.
- [6] Francesco Aieta, Patrice Genevet, Mikhail A Kats, Nanfang Yu, Romain Blanchard, Zeno Gaburro, and Federico Capasso. Aberration-free ultrathin flat lenses and axicons at telecom wavelengths based on plasmonic metasurfaces. *Nano letters*, 12(9):4932–4936, 2012.
- [7] Fan Yang, Hung-I Lin, Mikhail Shalaginov, Juejun Hu, and Tian Gu. Metasurface optics enabled computational sensing. In *AI and Optical Data Sciences IV*, volume 12438, pages 60–67. SPIE, 2023.
- [8] Paul R West, James L Stewart, Alexander V Kildishev, Vladimir M Shalaev, Vladimir V Shkunov, Friedrich Strohendl, Yuri A Zakharenkov, Robert K Dodds, and Robert Byren. All-dielectric subwavelength metasurface focusing lens. *Optics express*, 22(21):26212–26221, 2014.
- [9] Mohammadreza Khorasaninejad and Federico Capasso. Metalenses: Versatile multifunctional photonic components. *Science*, 358(6367):eaam8100, 2017.
- [10] Philippe Lalanne and Pierre Chavel. Metalenses at visible wavelengths: past, present, perspectives. *Laser & Photonics Reviews*, 11(3):1600295, 2017.
- [11] Ming Lun Tseng, Hui-Hsin Hsiao, Cheng Hung Chu, Mu Ku Chen, Greg Sun, Ai-Qun Liu, and Din Ping Tsai. Metalenses: advances and applications. *Advanced Optical Materials*, 6(18):1800554, 2018.
- [12] Tian Gu, Hyun Jung Kim, Clara Rivero-Baleine, and Juejun Hu. Reconfigurable metasurfaces towards commercial success. *Nature Photonics*, 17(1):48–58, 2023.
- [13] Qingbin Fan, Mingze Liu, Cheng Yang, Le Yu, Feng Yan, and Ting Xu. A high numerical aperture, polarization-insensitive metalens for long-wavelength infrared imaging. *Applied Physics Letters*, 113(20):201104, 2018.
- [14] Luocheng Huang, Zachary Coppens, Kent Hallman, Zheyi Han, Karl F Böhringer, Neset Akozbek, Ashok Raman, and Arka Majumdar. Long wavelength infrared imaging under ambient thermal radiation via an all-silicon metalens. *Optical Materials Express*, 11(9):2907–2914, 2021.



- [15] Junwei Li, Yilin Wang, Shengjie Liu, Ting Xu, Kai Wei, Yudong Zhang, and Hao Cui. Largest aperture metalens of high numerical aperture and polarization independence for long-wavelength infrared imaging. *Optics Express*, 30(16):28882–28891, 2022.
- [16] Mingming Hou, Yan Chen, and Fei Yi. Lightweight long-wave infrared camera via a single 5-centimeter-aperture metalens. In *CLEO: QELS Fundamental Science*, page FM4F.4. Optica Publishing Group, 2022.
- [17] Dongzhi Shan, Nianxi Xu, Jinsong Gao, Naitao Song, Hai Liu, Yang Tang, Xiaoguo Feng, Yansong Wang, Yi Zhao, Xin Chen, et al. Design of the all-silicon long-wavelength infrared achromatic metalens based on deep silicon etching. *Optics Express*, 30(8):13616–13629, 2022.
- [18] Esther M Conwell. Properties of silicon and germanium. *Proceedings of the IRE*, 40(11):1327–1337, 1952.
- [19] Halil Can Nalbant, Fatih Balli, Tolga Yelboğa, Arda Eren, and Ahmet Sözak. Transmission optimized lwir metalens. *Applied Optics*, 61(33):9946–9950, 2022.
- [20] Anna Wirth-Singh, Johannes E Frösch, Zheyi Han, Luocheng Huang, Saswata Mukherjee, Zhihao Zhou, Zachary Coppens, Karl F Böhringer, and Arka Majumdar. Large field-of-view thermal imaging via all-silicon meta-optics. *arXiv preprint arXiv:2304.14569*, 2023.
- [21] Chenglong Zhao, Ziqi Liu, and Wei Huang. Wide field-of-view metalens array for the long-wavelength infrared. In *Conference on Infrared, Millimeter, Terahertz Waves and Applications (IMT2022)*, volume 12565, pages 746–749. SPIE, 2023.
- [22] Mingbo Pu, Xiong Li, Yinghui Guo, Xiaoliang Ma, and Xiangang Luo. Nanoapertures with ordered rotations: symmetry transformation and wide-angle flat lensing. *Optics Express*, 25(25):31471–31477, 2017.
- [23] Augusto Martins, Kezheng Li, Juntao Li, Haowen Liang, Donato Conteduca, Ben-Hur V Borges, Thomas F Krauss, and Emiliano R Martins. On metalenses with arbitrarily wide field of view. *ACS Photonics*, 7(8):2073–2079, 2020.
- [24] Cong Chen, Panpan Chen, Jianxin Xi, Wanxia Huang, Kuanguo Li, Li Liang, Fenghua Shi, and Jianping Shi. On-chip monolithic wide-angle field-of-view metalens based on quadratic phase profile. *AIP Advances*, 10(11):115213, 2020.
- [25] Wen-peng Zhang, Fei Liang, Ya-rong Su, Ke Liu, Ming-jun Tang, Ling Li, Zheng-wei Xie, and Wu-ming Liu. Numerical simulation research of wide-angle beam steering based on catenary shaped ultrathin metalens. *Optics Communications*, 474:126085, 2020.
- [26] Emmanuel Lassalle, Tobias WW Mass, Damien Eschimese, Anton V Baranikov, Egor Khaidarov, Shiqiang Li, Ramon Paniagua-Dominguez, and Arseniy I Kuznetsov. Imaging properties of large field-of-view quadratic metalenses and their applications to fingerprint detection. *ACS Photonics*, 8(5):1457–1468, 2021.
- [27] Guangzhu Zhou, Shi-Wei Qu, Baojie Chen, Yuansong Zeng, and Chi Hou Chan. Metasurface-based fourier lens fed by compact plasmonic optical antennas for wide-angle beam steering. *Optics Express*, 30(12):21918–21930, 2022.
- [28] Ning Zhang, Qingzhi Li, Jun Chen, Feng Tang, Jingjun Wu, Xin Ye, and Liming Yang. Design of an all-dielectric long-wave infrared wide-angle metalens. *Chinese Physics B*, 31(7):074212, 2022.
- [29] Amir Arbabi, Ehsan Arbabi, Seyedeh Mahsa Kamali, Yu Horie, Seunghoon Han, and Andrei Faraon. Miniature optical planar camera based on a wide-angle metasurface doublet corrected for monochromatic aberrations. *Nature Communications*, 7:13682, 2016.
- [30] Benedikt Groever, Wei Ting Chen, and Federico Capasso. Meta-lens doublet in the visible region. *Nano letters*, 17(8):4902–4907, 2017.
- [31] Zhenyu Huang, Maosen Qin, Xiaowei Guo, Cheng Yang, and Shaorong Li. Achromatic and wide-field metalens in the visible region. *Optics Express*, 29(9):13542–13551, 2021.
- [32] Augusto Martins, Juntao Li, Ben-Hur V Borges, Thomas F Krauss, and Emiliano R Martins. Fundamental limits and design principles of doublet metalenses. *Nanophotonics*, 11(6):1187–1194, 2022.
- [33] Dongliang Tang, Long Chen, Jia Liu, and Xiaohu Zhang. Achromatic metasurface doublet with a wide incident angle for light focusing. *Optics Express*, 28(8):12209–12218, 2020.
- [34] Changhyun Kim, Sun-Je Kim, and Byoung-ho Lee. Doublet metalens design for high numerical aperture and simultaneous correction of chromatic and monochromatic aberrations. *Optics Express*, 28(12):18059–18076, 2020.
- [35] Fan Yang, Mikhail Y Shalaginov, Hung-I Lin, Sensong An, Anu Agarwal, Hualiang Zhang, Clara Rivero-Baleine, Tian Gu, and Juejun Hu. Wide field-of-view metalens: a tutorial. *Advanced Photonics*, 5(3):033001–033001, 2023.

- 
- [36] Mikhail Y Shalaginov, Sensong An, Fan Yang, Peter Su, Dominika Lyzwa, Anuradha M Agarwal, Hualiang Zhang, Juejun Hu, and Tian Gu. Single-element diffraction-limited fisheye metalens. *Nano Letters*, 20(10):7429–7437, 2020.
- [37] Fan Yang, Sensong An, Mikhail Y Shalaginov, Hualiang Zhang, Clara Rivero-Baleine, Juejun Hu, and Tian Gu. Design of broadband and wide-field-of-view metalenses. *Optics Letters*, 46(22):5735–5738, 2021.
- [38] Mikhail Y Shalaginov, Hung-I Lin, Fan Yang, Drew M Weninger, Crystal Li, Anuradha M Agarwal, Juejun Hu, and Tian Gu. Metasurface-enabled wide-angle stereoscopic imaging. In *Frontiers in Optics*, pages JTU7B–2. Optica Publishing Group, 2022.
- [39] Fan Yang, Sensong An, Mikhail Y Shalaginov, Hualiang Zhang, Juejun Hu, and Tian Gu. Understanding wide field-of-view flat lenses: an analytical solution. *Chinese Optics Letters*, 21(2):023601, 2023.
- [40] Mikhail Y Shalaginov, Sensong An, Yifei Zhang, Fan Yang, Peter Su, Vladimir Liberman, Jeffrey B Chou, Christopher M Roberts, Myungkoo Kang, Carlos Rios, et al. Reconfigurable all-dielectric metalens with diffraction-limited performance. *Nature communications*, 12(1):1225, 2021.
- [41] Fan Yang, Hung-I Lin, Mikhail Y Shalaginov, Katherine Stoll, Sensong An, Clara Rivero-Baleine, Myungkoo Kang, Anuradha Agarwal, Kathleen Richardson, Hualiang Zhang, et al. Reconfigurable parfocal zoom metalens. *Advanced Optical Materials*, 10(17):2200721, 2022.